Letter

Nonlinear Bragg interferometer with a trapped Bose-Einstein condensate

Robin Corgier, Luca Pezzè and Augusto Smerzi
QSTAR, INO-CNR, and LENS, Largo Enrico Fermi 2, 50125 Firenze, Italy

(Received 15 January 2021; accepted 5 April 2021; published 9 June 2021)

We propose a scheme for trapped-atom interferometry using an interacting Bose-Einstein condensate. The condensate is controlled and spatially split into two confined external momentum modes through a series of Bragg pulses. The proposed scheme (i) allows the generation of large entanglement in a trapped-interferometer configuration via one-axis twisting dynamics induced by interatomic interaction and (ii) avoids the suppression of interactions during the interferometer sequence by a careful manipulation of the state before and after phase encoding. The interferometer can be used for the measurement of gravity with a sensitivity beyond the standard quantum limit.

DOI: 10.1103/PhysRevA.103.L061301

I. INTRODUCTION

Matter-wave atom interferometers are ideal tools for inertial measurements [1,2]: they enable tests of fundamental theories [3–8], as well as practical applications [9] such as gravimeters [10–14], gradiometers [15–17], and gyroscopes [18–23]. In the wider context of grand unification theory [24], dual-species matter-wave atom interferometer have been proposed to test in a unique way the weak equivalence principle [25–29] where gravity can be tested within a quantum framework competing with state-of-the-art classical technologies [30–32]. The use of entangled probe states [33–35] has been proposed as a viable method to increase the sensitivity of atom interferometers beyond the standard quantum limit (SQL) imposed by uncorrelated-atom probes [36–44]. However, so far, sub-SQL sensitivities have been mainly shown in proof-of-principle experiments [36] that might not be compatible with the strict experimental conditions imposed by the specific application [45]. For instance, gravimeters require the creation of entangled atoms in controllable and separable momentum modes [46]. To generate such states, recent proposals explored the use of high-finesse optical cavities [47–49] or particle-particle interaction in Bose-Einstein condensates (BECs) where entanglement into internal levels is converted to external degrees of freedom via Raman addressing [37,50].

In this paper we propose a trapped-atom interferometer for the measurement of inertial forces and gravity with a sensitivity beyond the SQL. The interferometer uses a trapped interacting BEC with beam splitters implemented by Bragg pulses [51–53] (see Fig. 1). Particle entanglement is generated in trapped momentum modes via elastic atom-atom interaction, which is kept in the interferometer sequence. We show that sub-SQL sensitivities can be reached, in our scheme [also referred to as a nonlinear atom interferometer (NLAI)], due to a careful rotation of the state before and after the interferometer sequence that accounts for the growth of phase fluctuations generated by interatomic collisions. This avoids the exploitation of a Feshbach resonance to suppress the scattering length between BEC atoms [38] during the interferometer operations, which may introduce substantial systematic effects [54,55]. It thus paves the way toward practical applications of ultrasensitive trapped-atom interferometry.

II. INTERFEROMETER SCHEME

The atom interferometer discussed in this paper is shown schematically in Fig. 1. It starts with a BEC of N atoms initially at rest in the bottom of a harmonic dipole potential. The trap is kept on during the full interferometer process, until the final readout. At $t = 0$, a Bragg pulse coherently splits the BEC in two momentum states $\pm\hbar k_0$, where the effective wave vectors correspond to the two-photon transition $k_0 = 2k_L$. Each particle in the BEC is in a quantum superposition of momenta $\pm\hbar k_0$ such that the state after the Bragg pulse is described by the coherent spin state $|\psi_{\rm in}\rangle = 2^{-S}\sum_{n=-S}^{S}\binom{2S}{S+n}^{1/2}|S+n, S-n\rangle$, with $S = N/2$ and the state $|S+n, S-n\rangle$ indicating $S \pm n$ atoms with momenta $\pm\hbar k_0$, respectively. Notice that we neglect the possible extra momentum mode generated at each laser pulse [53,56]. To this aim, different configurations can be considered, such as double Bragg pulses [52] or the combination of an optical lattice and single Bragg pulses [51,53]. Here we assume an infinitely narrow momentum distribution of the input state and justify the use of BECs instead of a thermal ensemble [57].

The system is described by the field operator $\hat{\Psi}(\mathbf{r}, t) = \Phi_+(\mathbf{r}, t)\hat{a}_+ + \Phi_-(\mathbf{r}, t)\hat{a}_-$, where $\Phi_\pm(\mathbf{r}, t)$ carry the spatial evolution of the two mean-field wave functions and $\hat{a}_\pm$ ($\hat{a}_\pm^\dagger$) is the bosonic annihilation (creation) operator of the $\pm\hbar k_0$ mode. It is convenient to introduce the SU(2) pseudospin operators of the Lie algebra [58] $\hat{S}_x = (\hat{a}_+^\dagger\hat{a}_- + \hat{a}_-^\dagger\hat{a}_+)/2$, $\hat{S}_y = (\hat{a}_+^\dagger\hat{a}_- - \hat{a}_-^\dagger\hat{a}_+)/2i$, and $\hat{S}_z = (\hat{a}_+^\dagger\hat{a}_+ - \hat{a}_-^\dagger\hat{a}_-)/2$, satisfying the commutation relation $[S_i, S_j] = i\epsilon_{ijk}S_k$, with ϵ_{ijk} the Levi-Cività symbol. Bragg pulses, considered instantaneous at a particu-

 ©2021 American Physical Society

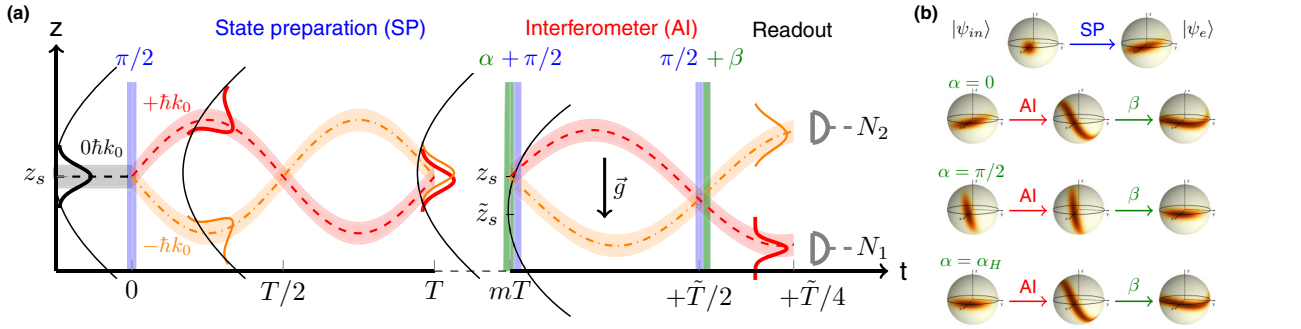

FIG. 1. (a) Scheme of the trapped interferometer. At $t=0$, a $\pi/2$ Bragg pulse (vertical blue $\pi/2$ pulse) splits the BEC in two momentum modes. The state preparation consists of back-and-forth oscillations up to the time $t=mT$ and is optimized by a final α pulse (vertical green α pulse). A $\pi/2$ Bragg pulse starts the interferometer sequence. To be sensitive to gravity, the trap frequency is changed from ω_z to $\tilde{\omega}_z$. The final $\pi/2$ Bragg pulse closes the interferometer and the state is further optimized by a β pulse (vertical green α pulse). The phase is measured by counting the number of atoms in each cloud at time $t=mT+3\tilde{T}/4$, when the two output modes are separated and the trap is turn off. (b) Main steps of the sequence shown in a Husimi Q distribution on the Bloch sphere. The top row shows the initial coherent spin state at $t=0$ and the generated spin-squeezed state at $t=mT$. The next three rows show the state at different stages of the interferometer: after the α rotation (left column), after phase accumulation (center column), and after β rotation optimization (right column). Here α_H denotes the optimal rotation of the state in the case of a linear interferometer sequence.

lar time t_p, are characterized by an effective Rabi frequency Ω_R and phase ϕ_L and are described by the linear Hamiltonian $\hat{H}_0(t)=\hbar\Omega_R\delta(t-t_p)[\cos(\phi_L)\hat{S}_x+\sin(\phi_L)\hat{S}_y]+\hbar\delta\theta\hat{S}_z$, where $\delta(t-t_p)$ is the Dirac delta function and $\delta\theta$ is the precession of the state due to the phase accumulation. Interatomic interaction in the BEC is responsible for generation of entanglement between the particles. The interaction is described by $\hat{H}_{\rm int}(t)=\hbar\chi(t)\hat{S}_z^2$, where the time dependence in the coefficient $\chi(t)$ is associated with the dynamics of the wave function in the trap.

During the state preparation, no phase is accumulated and the state is described by the one-axis-twisting [59] evolution

$$|\psi_e(mT)\rangle=e^{-i\tau_m\hat{S}_z^2}|\psi_{\rm in}\rangle, \tag{1}$$

where $\tau_m=\int_0^{mT}\chi(t)dt$ is the accumulated nonlinear coefficient after a time mT depending on the dynamics of the wave packets $\Phi_\pm$ in the trap, $T=2\pi/\omega_z$, and ω_z is the angular trap frequency [60]. The calculation of τ_m can be simplified by neglecting the recombination of the mode at each half-period of the trap, giving

$$\tau_m^{\rm S}=\frac{2m\pi}{7}\left(15a\gamma^2\sqrt{\frac{M}{\hbar}}\right)^{2/5}\left(\frac{\omega_z}{N^3}\right)^{1/5}, \tag{2}$$

where a denotes the particle-particle s-wave scattering length, M is the mass of the atom, $\omega_{x,y,z}$ are the trap frequencies, $\hbar$ is the Plank constant, and $\gamma=\omega_{x,y}/\omega_z$ is the trap aspect ratio. In practice, a fine-tuning of τ_m can be obtained by changing γ and ω_z. Furthermore, $\tau_m^{\rm S}$ linearly increases with the number m of back-and-forth oscillations of the two spatial modes in the trap (see Fig. 1). In Fig. 2 we compare τ_m with the approximated $\tau_m^{\rm S}$ for the case $m=1/2$, as a function of the trap frequency [Fig. 2(a)] and trap aspect ratio [Fig. 2(b)] [60]. For relatively short times, the entangling evolution (1) can generate a substantial amount of spin squeezing in the state $|\psi_e(mT)\rangle$. This corresponds to the state having spin fluctuations $(\Delta\hat{S}_z)^2$ smaller than the value $N/4$ of uncorrelated atoms while retaining a large coherence length $\langle\hat{S}_x^2\rangle+\langle\hat{S}_y^2\rangle\approx N^2/4$. When plotted in the Bloch sphere, the spin-squeezed states have a characteristic ellipsoid distribution, as shown in Fig. 1(b). If the state is rotated around the direction y, perpendicular to the squeezed direction, it becomes distinguishable after a rotation angle $\theta<1/\sqrt{N}$ [36,61], namely, below the SQL that characterizes the state distinguishability of coherent spin states under the same rotation. Metrologically useful spin squeezing can be quantified by the Wineland parameter $\xi^2=N(\Delta\hat{S}_z)^2/(\langle\hat{S}_x\rangle^2+\langle\hat{S}_y\rangle^2)$ [62]. In particular, the horizontal dot-dashed lines in Fig. 2 denote $\tau_{\rm opt}\approx 1.2/N^{2/3}$, leading to the minimum value $\min[\xi(\tau_{\rm opt})]=N^{-1/3}$ [33]. It is important to compare our scheme with that of Ref. [37], where entanglement has been generated between a two-component BEC (different internal state of ^{87}Rb addressed by Raman transitions; see also [50]) due to a state-dependent potential. Here entanglement is generated between two different momentum states of a single-component BEC (same internal

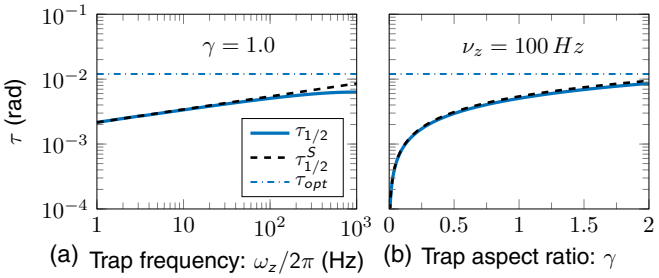

FIG. 2. Input state preparation. Accumulated nonlinear coefficient $\tau_{1/2}$ (a) as a function of ω_z and for spherical trap ($\gamma=1$) and (b) as a function of the trap aspect ration γ, ranging from a pancake geometry ($\gamma<1$) to a cylindrical geometry ($\gamma>1$). The solid, dashed, and dot-dashed lines show $\tau_{1/2}$, $\tilde{\tau}$, and $\tau_{\rm opt}$, respectively.

state) where the overlap of the two modes does not inhibit the generation of squeezing.

The interferometer operation consists of two Bragg pulses at times mT and $mT + \tilde{T}/2$, described by $R_x(\pi/2) = e^{-i\pi/2\hat{S}_x}$ and $R_x^\dagger(\pi/2)$, respectively. In between, the angular trap frequency is changed from ω_z to $\tilde{\omega}_z$, with $\tilde{T} = 2\pi/\tilde{\omega}_z$ indicating the period of the new trap (see Fig. 1). In this configuration the phase accumulated after half a period is $\theta = 2k_0 g(1/\tilde{\omega}_z^2 - 1/\omega_z^2)$ [63,64], which makes the apparatus sensitive to gravity. Furthermore, the initial (final) pulse can be combined with a rotation of angles α (β) in order to optimize the state [59] [see the discussion below and Fig. 1(b)] and combat the degradation due to phase diffusion [65]. Using $R_x^\dagger(\pi/2)e^{-i(\tilde{\tau}\hat{S}_z^2+\theta\hat{S}_z)}R_x(\pi/2) = e^{-i(\tilde{\tau}\hat{S}_y^2+\theta\hat{S}_y)}$, the final state of the full interferometer sequence is described by the transformation

$$|\psi_f\rangle = e^{-i\beta\hat{S}_x}e^{-i(\tilde{\tau}\hat{S}_y^2+\theta\hat{S}_y)}e^{-i\alpha\hat{S}_x}|\psi_e(mT)\rangle, \tag{3}$$

where $\tilde{\tau} \neq 0$ denotes the accumulated extra nonlinear coefficient during the interferometer sequence.

The nonlinear parameters τ_m (for state preparation) and $\tilde{\tau}$ (for the interferometer sequence) can be tuned independently of each other. Note that the current trapped interferometer sequence avoids the characteristic refocusing π pulse of free-falling atom interferometers: the refocusing is provided by the trap geometry. At the end of the interferometer sequence, the BEC is kept in the trap for an extra time $\tilde{T}/4$ that guarantees maximum separation between the wave packets. After that, the BEC is released from the trap and imaged. The phase is estimated by inverting the sinusoidal relation between θ and the average relative number of particles at the output ports. In the following we study the sensitivity gain $\mathcal{G}_{\alpha,\beta}$ of the nonlinear atom interferometer sequence of Fig. 1 with respect to the standard quantum limit $\Delta\theta_{\mathrm{SQL}} = 1/\sqrt{N}$ [66]. Here $\Delta\theta = \Delta\theta_{\mathrm{SN}}/\mathcal{G}_{\alpha,\beta}$ is the phase sensitivity of the NLAI, where $(\Delta\theta)^2 = (\Delta S_z)^2_{\alpha,\beta}/(d\langle S_z\rangle_{\alpha,\beta}/d\theta)^2$ is obtained by error propagation and the spin moments are calculated for the output state of Eq. (3). In particular, for $\theta = 0$ we have [66]

$$\mathcal{G}^2_{\alpha,\beta} = \frac{\langle\hat{S}_x\rangle^2_{\alpha,\beta}}{N(\Delta\hat{S}_z)^2_{\alpha,\beta}}\cos^2\beta. \tag{4}$$

The indices α and β refer to the rotation of the state on the Bloch sphere before and after the interferometer sequence [see Eq. (3)]. In the following, the parameter β is always optimized to maximize the sensitivity gain while we consider different choices of α: $\alpha = 0, \pi/2, \alpha_H$, and α_{opt}. The first two choices lead to a total of $\pi/2$ and π pulses, respectively, at time $t = mT$ and can easily be implemented experimentally. The case $\alpha = \alpha_H$ refers to the optimal rotation in the case of a linear interferometer sequence and $\alpha = \alpha_{\mathrm{opt}}$ refers to a state protection strategy used to limit the impact of $\tilde{\tau}$. In the following we denote by $\mathcal{G}^L_{\alpha_H} = \min[\xi]$ the optimal sensitivity gain of a linear interferometer ($\tilde{\tau} = 0$).

III. WEAK NLAI

We first study analytically the situation where $\tilde{\tau}$ is small enough to approximate $e^{-i\tilde{\tau}\hat{S}_y^2} \approx 1 - i\tilde{\tau}\hat{S}_y^2$. For $\theta = 0$, we can rewrite Eq. (4) as [66]

$$\mathcal{G}^2_{\alpha,\beta} = (1 + (2S-1)\{\sin(2\beta)\tilde{\tau} - \sin[2(\alpha+\beta)]\tau\})\cos^2\beta. \tag{5}$$

In the case $\alpha = 0$, the nonlinear evolution during the interferometer sequence degrades the sensitivity gain by "unsqueezing" the state though the term $\sin(2\beta)(\tilde{\tau} - \tau)$. In contrast, for $\alpha = \pi/2$, the contribution of $\tilde{\tau}$ adds to τ such that the nonlinear evolution during the interferometer "squeezes" the state even further though the term $\sin(2\beta)(\tilde{\tau} + \tau)$. In this configuration the total pulse at time mT reads $R_x(\pi)$ where the input spin-squeezed state is rotated by π around $\hat{S}_x$. The total amount of nonlinearity can then be simply described by $e^{-i(\tau+\tilde{\tau})\hat{S}_z^2}$ where the π pulse at time $t = mT$ does not change the orientation of the spin-squeezed state on the Bloch sphere. Nevertheless, in both cases the sensitivity gain $\mathcal{G}_{\alpha,\beta}$ is strongly impacted in general for $\beta \neq 0$ through the term $\cos^2\beta$ of Eq. (4). In the case $\beta = 0$, the nonlinear evolution during the interferometer does not play a role and for $\pi/2 < \alpha < \pi$ the sensitivity is sub-SQL. This configuration is equivalent to a linear interferometer sequence optimized for $\alpha_H = -\pi/4$. The fact that the different rotations do not lead to the same maximum gain emphasizes the importance of a careful prerotation and postrotation of the state to reach $\mathcal{G} > 1$.

IV. STRONG NLAI

We now study numerically the more realistic case where the nonlinear terms of the state preparation and interferometer sequence are not small. Figure 3 shows the sensitivity gain as a function of the number of back-and-forth oscillations m and for different trap aspect ratios. Let us first discuss the case of weak interaction, namely, γ and m small and $\tau \ll \tau_{\mathrm{opt}}$. In the case of $\alpha = \alpha_H$, the results confirm qualitatively the analysis discussed above where $\mathcal{G}_{\alpha_H,\beta_{\mathrm{opt}}} \approx \mathcal{G}^L_{\alpha_H}$. It is interesting to note that the case $\alpha = 0$ gives results very similar to a numerical optimizations over both α and β (green stars): $\mathcal{G}_{0,\beta_{\mathrm{opt}}} \approx \mathcal{G}_{\alpha_H,\beta_{\mathrm{opt}}} \approx \mathcal{G}^L_{\alpha_{\mathrm{opt}}}$. This configuration corresponds indeed to an effortless strategy where only the strength of the final Bragg pulse, closing the interferometer, needs to be scanned (and optimized). For $\alpha = 0$ the state is given by $|\psi_f\rangle = e^{-i\beta\hat{S}_x}e^{-i\tilde{\tau}\hat{S}_y^2}e^{-i\tau\hat{S}_z^2}|\psi_{\mathrm{in}}\rangle$, where the sequential action of first $e^{-i\tau\hat{S}_z^2}$ and then $e^{-i\tilde{\tau}\hat{S}_y^2}$ on the state shears the ellipsoid into two different directions, leading to the S shape highlighted in Fig. 1(b) on the Bloch sphere. In the case where $\alpha = \pi/2$ the state reads $|\psi_f\rangle = e^{-i(\beta+\pi/2)\hat{S}_x}e^{-i(\tilde{\tau}+\tau)\hat{S}_z^2}|\psi_{\mathrm{in}}\rangle$. As shown in Fig. 1(b), in this case the ellipsoid is not deformed and does not exhibit an S shape. Even though the orientation of the state can be optimized though the β rotation, the sensitivity of the interferometer is strongly degraded for $\beta \neq 0$ [see Eq. (4)]. This supports the results of Fig. 3 showing that, in this case, the sensitivity is at the best the SQL (blue curve).

In the case of a strong interaction, namely, γ and m large, the nonlinear term $\tilde{\tau}$ dramatically degrades the sensitivity gain. In this configuration a nontrivial rotation of the input state is needed ($\alpha \neq 0$ and $\alpha \neq \alpha_H$) and a trade-off between the deformation of the ellipsoid, S shape, and final rotation

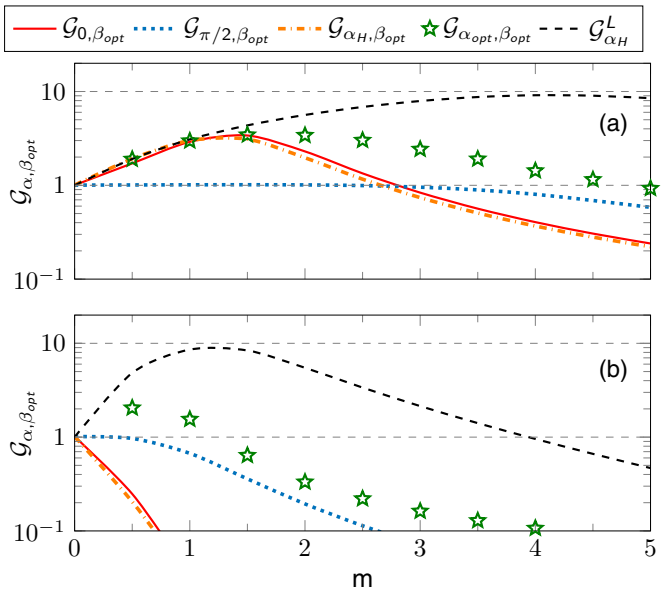

FIG. 3. Gain factor $\mathcal{G}_{\alpha,\beta_{\rm opt}}$ as a function of m (namely, for different spin-squeezed input states) for trap aspect ratios (a) $\gamma = 0.2$ (pancake shape) and (b) $\gamma = 1$ (spherical shape). The different lines refer to a linear interferometer (black dashed lines) and nonlinear interferometer sequence (colored lines) with $\alpha = 0$ (red), $\pi/2$ (blue), α_H (orange), and $\alpha_{\rm opt}$ (green stars). The numerical results have been calculated for $m = 0, 1/2, 1, \ldots$ and curves are a guide to the eye obtained via spline interpolation. The maximum gain $\mathcal{G}_{\rm max} = \max_\tau[\mathcal{G}^L_{aH}(\tau)] = N^{1/3}$ and SQL $\mathcal{G} = 1$ are highlighted by the horizontal dashed lines.

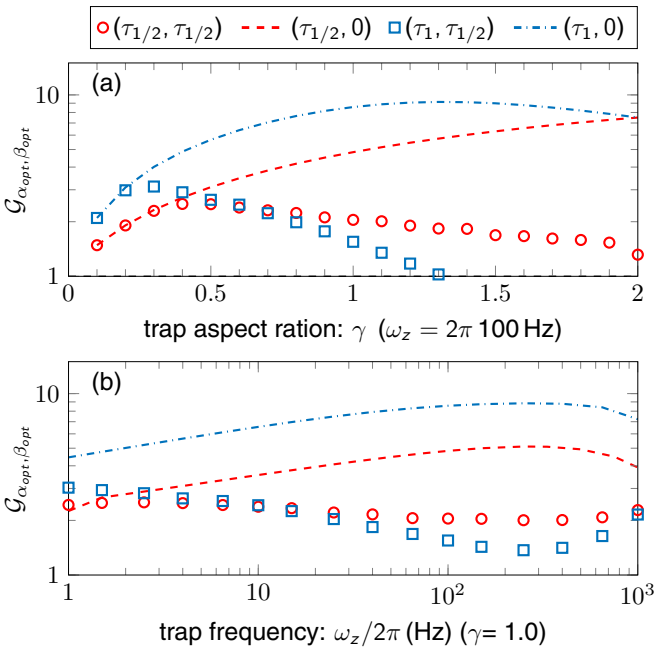

FIG. 4. Optimized gain factor $\mathcal{G}_{\alpha_{\rm opt},\beta_{\rm opt}}$ (a) as a function of the trap aspect ratio and for a fixed trap frequency $\nu_z = 100$ Hz and (b) as a function of the trap frequency for a spherical trap $\gamma = 1$. Red and blue symbols are obtained for a nonlinear interferometer with $m = 1/2$ ($\tau = \tau_{1/2}$) and $m = 1$ ($\tau = \tau_1$), respectively. The dashed lines denote the corresponding sensitivity for a linear interferometer where $\tilde{\tau} = 0$.

$\beta \neq 0$ degrading the sensitivity gain is required to reach a sub-SQL sensitivity (green stars).

Figure 4 shows the sensitivity gain optimized with respect to α and β for different trap aspect ratios [Fig. 4(a)] and trap frequencies [Fig. 4(b)] in the case where the input spin-squeezed state is generated by $m = 1/2$ (red) or $m = 1$ (blue) back-and-forth oscillations. In both cases, increasing the number of back-and-forth oscillations increases the maximum sensitivity gain, where the nonlinear terms are controlled through the different trap parameters. Indeed, even if $\tau_{1/2}$ is small, after m back-and-forth oscillations $\tau_m = 2m\tau_{1/2}$ while $\tilde{\tau} = \tau_{1/2}$. The oscillation of the maximum sensitivity gain, shown in Fig. 4(b), is a direct consequence of the trade-off discussed above. In the case of high trap frequencies and oversqueezed input spin-squeezed states (namely, $\tau > \tau_{\rm opt}$), the nonlinear term $\tilde{\tau}$ can unsqueeze the state, explaining the sudden increase of the optimized sensitivity gain at high trap frequency observed in Fig. 4(b).

V. DISCUSSION

Let us give some details on the sensitivity of the trapped interferometer used for a gravity measurement. In this case the phase accumulated between the two arms is given by $\theta = (2k_0)g(\tilde{T}/4)^2$ [63], where, in analogy to a free-fall Mach-Zehnder interferometer sequence, $\tilde{T}/4$ denotes the time between the different pulses. As a result, the single-shot gravity sensitivity is directly related to the phase sensitivity gain through

$$\Delta g = \frac{4\Delta\theta_{\rm SQL}}{\mathcal{G}_{\alpha,\beta} k_L \tilde{T}^2}. \tag{6}$$

Considering the case of a ^{87}Rb BEC of $N = 10^3$ in an $\omega_z = 2\pi \times 50$ Hz trap along the vertical direction, $k_L = 2\pi/\lambda_L$, $\lambda_L = 852$ nm, and a maximum sensitivity gain of $\mathcal{G}_{\rm max} = N^{1/3}$, one could reach a sensitivity of $\Delta g/g \approx 5 \times 10^{-7}$ per shot. Using a coherent spin state as a probe, namely, in the absence of the squeezed-state preparation sequence, an equivalent result would require a BEC of $N = 10^5$ atoms. Nevertheless, in this case the impact of interaction during the different laser pulses would generate extra modes degrading the sensitivity of the interferometer.

Above, we have assumed a perfectly harmonic trap configuration. Indeed, nonharmonic traps (magnetic or optic) do not prohibit the two modes from overlapping but could induce a nonidentical shape deformation of each mode, limiting therefore the efficiency of the different Bragg pulses. Nevertheless, one can expect that the different back-and-forth oscillations would impact the shape of each mode in a similar manner, on average limiting the detrimental effect of a shape deformation. Furthermore, it has been shown that the problem of mode mismatch at the end of the interferometer can as well be adjusted through a careful rotation of the state [67]. In addition, in the case of a dipole trap configuration large harmonic traps can be accessible though the painted potential technique at the cost of laser power [68,69].

We have also considered a constant number of atoms while, in practice, the shot-to-shot fluctuation in atom number between two consecutive runs cannot be avoided. Such fluctuations can be dramatic in regard to the full optimization of the interferometer sequence where the pre- and post- of the state are directly linked to the number of atoms. In addition, the intensity of the laser, the phase of the Bragg pulses, and the trap frequencies have been assumed to be identical for each experimental run. Experimental drift of these quantities would lead to an imperfect splitting process, imperfect manipulation of the state, and extra mode mismatch at the end of the interferometer, degrading the sensitivity of the interferometer. In this paper we have shown that, in the regime of weak interactions ($N = 10^3$ atoms in a $2\pi\{20, 20, 100\}$ Hz trap), the prerotation of the state can be avoided ($\alpha = 0$) in order to reach the best sensitivity gain $\mathcal{G}_{0,\beta_{\rm opt}} = 3.5$. Here the BEC is described through a variational approach where the shape of the mode is assumed to be a Gaussian with a constant shape for simplicity (a more advanced numerical approach is required for a more quantitative experimental description). Weakly interacting BECs are required since strong interactions lead to inefficient beam splitters [70] and to the creation of extra modes [50,71]. Non-negligible initial momentum spread would lead to the same detrimental effects [53,56,57]. Furthermore, BEC collisions at each half-period of oscillations may induce detrimental effects [72]. A detailed study of the dynamical wave packets in the trapped interferometer is beyond the scope of this paper.

VI. CONCLUSION

The trapped-atom interferometer proposed in this paper reaches sub-SQL sensitivities without requiring the suppression of the particle-particle scattering length during phase encoding. The presence of nonlinearity during the interferometer operations can be mitigated via optimal rotations of the state on the Bloch sphere. Our result are supported by analytical calculations in the regime of weak interaction and numerically in the regime of strong interactions. Larger trap aspect ratios and/or weaker trap frequencies accessible today in the microgravity environment [73,74] would benefit from the proposed interferometer where arbitrary input spin-squeezed states could be made available but not impacted by a nonlinear interferometer sequence. The strategy proposed is consistent with the current technology development and feasibility in current laboratory experiments [37], where only the final beam splitter has to be optimized to exhibit sub-SQL sensitivity measurements.

ACKNOWLEDGMENTS

The authors thank Carsten Klempt, Naceur Gaaloul, Alessia Burchianti, Chiara d'Errico, Marco Fattori, Chiara Fort, Francesco Minardi, and Samuel Nolan for fruitful discussions. This work was supported by the European Unions Horizon 2020 research and innovation program, Qombs Project, FET Flagship on Quantum Technologies Grant No. 820419.

[1] B. Canuel, F. Leduc, D. Holleville, A. Gauguet, J. Fils, A. Virdis, A. Clairon, N. Dimarcq, Ch. J. Bordé, A. Landragin, and P. Bouyer, Six-Axis Inertial Sensor Using Cold-Atom Interferometry, Phys. Rev. Lett. **97**, 010402 (2006).

[2] R. Geiger, A. Landragin, S. Merlet, and F. Pereira Dos Santos, High-accuracy inertial measurements with cold-atom sensors, AVS Quantum Sci. **2**, 024702 (2020).

[3] J. B. Fixler, G. T. Foster, J. M. McGuirk, and M. A. Kasevich, Atom interferometer measurement of the Newtonian constant of gravity, Science **315**, 74 (2007).

[4] G. Lamporesi, A. Bertoldi, L. Cacciapuoti, M. Prevedelli, and G. M. Tino, Determination of the Newtonian Gravitational Constant Using Atom Interferometry, Phys. Rev. Lett. **100**, 050801 (2008).

[5] P. W. Graham, J. M. Hogan, M. A. Kasevich, and S. Rajendran, New Method for Gravitational Wave Detection with Atomic Sensors, Phys. Rev. Lett. **110**, 171102 (2013).

[6] G. Rosi, F. Sorrentino, L. Cacciapuoti, M. Prevedelli, and G. M. Tino, Precision measurement of the Newtonian gravitational constant using cold atoms, Nature (London) **510**, 518 (2014).

[7] W. Chaibi, R. Geiger, B. Canuel, A. Bertoldi, A. Landragin, and P. Bouyer, Low frequency gravitational wave detection with ground-based atom interferometer arrays, Phys. Rev. D **93**, 021101(R) (2016).

[8] R. H. Parker, C. Yu, W. Zhong, B. Estey, and H. Müller, Measurement of the fine-structure constant as a test of the standard model, Science **360**, 191 (2018).

[9] K. Bongs, M. Holynski, J. Vovrosh, P. Bouyer, G. Condon, E. Rasel, C. Schubert, W. P. Schleich, and A. Roura, Taking atom interferometric quantum sensors from the laboratory to real-world applications, Nature Reviews Physics **1**, 731 (2019).

[10] A. Peters, K. Y. Chung, and S. Chu, Measurement of gravitational acceleration by dropping atoms, Nature (London) **400**, 849 (1999).

[11] J. E. Debs, P. A. Altin, T. H. Barter, D. Döring, G. R. Dennis, G. McDonald, R. P. Anderson, J. D. Close, and N. P. Robins, Cold-atom gravimetry with a Bose-Einstein condensate, Phys. Rev. A **84**, 033610 (2011).

[12] P. A. Altin, M. T. Johnsson, V. Negnevitsky, G. R. Dennis, R. P. Anderson, J. E. Debs, S. S. Szigeti, K. S. Hardman, S. Bennetts, G. D. McDonald, L. D. Turner, J. D. Close and N. P. Robins, Precision atomic gravimeter based on Bragg diffraction, New J. Phys. **15**, 023009 (2013).

[13] O. Francis, H. Baumann, T. Volarik, C. Rothleitner, G. Klein, M. Seil, N. Dando, R. Tracey, C. Ullrich, S. Castelein, H. Hua *et al.*, The European Comparison of Absolute Gravimeters 2011 (ECAG-2011) in Walferdange, Luxembourg: Results and recommendations, Metrologia **50**, 257 (2013).

[14] S. Abend, M. Gebbe, M. Gersemann, H. Ahlers, H. Müntinga, E. Giese, N. Gaaloul, C. Schubert, C. Lämmerzahl, W. Ertmer, W. P. Schleich, and E. M. Rasel, Atom-Chip Fountain Gravimeter, Phys. Rev. Lett. **117**, 203003 (2016).

[15] M. J. Snadden, J. M. McGuirk, P. Bouyer, K. G. Haritos, and M. A. Kasevich, Measurement of the Earth's Gravity Gradient

with an Atom Interferometer-Based Gravity Gradiometer, Phys. Rev. Lett. **81**, 971 (1998).

[16] J. M. McGuirk, G. T. Foster, J. B. Fixler, M. J. Snadden, and M. A. Kasevich, Sensitive absolute-gravity gradiometry using atom interferometry, Phys. Rev. A **65**, 033608 (2002).

[17] A. Trimeche, B. Battelier, D. Becker, A. Bertoldi, P. Bouyer, C. Braxmaier, E. Charron, R. Corgier, M. Cornelius, K. Douch, N. Gaaloul, S. Herrmann, J. Müller, E. Rasel, C. Schubert, H. Wu and F. Pereira, Concept study and preliminary design of a cold atom interferometer for space gravity gradiometry, Classical Quantum Grav. **36**, 215004 (2019).

[18] F. Riehle, T. Kisters, A. Witte, J. Helmcke, and C. J. Bordé, Optical Ramsey Spectroscopy in a Rotating Frame: Sagnac Effect in a Matter-Wave Interferometer, Phys. Rev. Lett. **67**, 177 (1991).

[19] T. L. Gustavson, P. Bouyer, and M. A. Kasevich, Precision Rotation Measurements with an Atom Interferometer Gyroscope, Phys. Rev. Lett. **78**, 2046 (1997).

[20] T. L. Gustavson, A. Landragin, and M. A. Kasevich, Rotation sensing with a dual atom-interferometer Sagnac gyroscope, Classical Quantum Grav. **17**, 2385 (2000).

[21] D. S. Durfee, Y. K. Shaham, and M. A. Kasevich, Long-Term Stability of an Area-Reversible Atom-Interferometer Sagnac Gyroscope, Phys. Rev. Lett. **97**, 240801 (2006).

[22] J. K. Stockton, K. Takase, and M. A. Kasevich, Absolute Geodetic Rotation Measurement Using Atom Interferometry, Phys. Rev. Lett. **107**, 133001 (2011).

[23] G. Tackmann, P. Berg, C. Schubert, S. Abend, M. Gilowski, W. Ertmer, and E. M. Rasel, Self-alignment of a compact large-area atomic Sagnac interferometer, New J. Phys. **14**, 015002 (2012).

[24] C. Kiefer, *Quantum Gravity* (Oxford University Press, Oxford, 2007).

[25] D. Schlippert, J. Hartwig, H. Albers, L. L. Richardson, C. Schubert, A. Roura, W. P. Schleich, W. Ertmer, and E. M. Rasel, Quantum Test of the Universality of Free Fall, Phys. Rev. Lett. **112**, 203002 (2014).

[26] L. Zhou, S. Long, B. Tang, X. Chen, F. Gao, W. Peng, W. Duan, J. Zhong, Z. Xiong, J. Wang, Y. Zhang, and M. Zhan, Test of Equivalence Principle at 10^{-8} Level by a Dual-Species Double-Diffraction Raman Atom Interferometer, Phys. Rev. Lett. **115**, 013004 (2015).

[27] B. Barrett, L. Antoni-Micollier, L. Chichet, B. Battelier, T. Lévèque, A. Landragin, and P. Bouyer, Dual matter-wave inertial sensors in weightlessness, Nat. Commun. **7**, 13786 (2016).

[28] X.-C. Duan, X.-B. Deng, M.-K. Zhou, K. Zhang, W.-J. Xu, F. Xiong, Y.-Y. Xu, C.-G. Shao, J. Luo, and Z.-K. Hu, Test of the Universality of Free Fall with Atoms in Different Spin Orientations, Phys. Rev. Lett. **117**, 023001 (2016).

[29] P. Asenbaum, C. Overstreet, M. Kim, J. Curti, and M. A. Kasevich, Atom-Interferometric Test of the Equivalence Principle at the 10^{-12} Level, Phys. Rev. Lett. **125**, 191101 (2020).

[30] J. G. Williams, S. G. Turyshev, and D. H. Boggs, Progress in Lunar Laser Ranging Tests of Relativistic Gravity, Phys. Rev. Lett. **93**, 261101 (2004).

[31] S. Schlamminger, K.-Y. Choi, T. A. Wagner, J. H. Gundlach, and E. G. Adelberger, Test of the Equivalence Principle Using a Rotating Torsion Balance, Phys. Rev. Lett. **100**, 041101 (2008).

[32] P. Touboul, G. Métris, M. Rodrigues, Y. André, Q. Baghi, J. Bergé, D. Boulanger, S. Bremer, P. Carle, R. Chhun, B. Christophe *et al.*, *MICROSCOPE* Mission: First Results of a Space Test of the Equivalence Principle, Phys. Rev. Lett. **119**, 231101 (2017).

[33] L. Pezzè and A. Smerzi, Entanglement, Nonlinear Dynamics, and the Heisenberg Limit, Phys. Rev. Lett. **102**, 100401 (2009).

[34] P. Hyllus, W. Laskowski, R. Krischek, C. Schwemmer, W. Wieczorek, H. Weinfurter, L. Pezzè, and A. Smerzi, Fisher information and multiparticle entanglement, Phys. Rev. A **85**, 022321 (2012).

[35] G. Tóth, Multipartite entanglement and high-precision metrology, Phys. Rev. A **85**, 022322 (2012).

[36] L. Pezzè, A. Smerzi, M. K. Oberthaler, R. Schmied, and P. Treutlein, Quantum metrology with nonclassical states of atomic ensembles, Rev. Mod. Phys. **90**, 035005 (2018).

[37] M. F. Riedel, P. Böhi, Y. Li, T. W. Hänsch, A. Sinatra, and P. Treutlein, Atom-chip-based generation of entanglement for quantum metrology, Nature (London) **464**, 1170 (2010).

[38] C. Gross, T. Zibold, E. Nicklas, J. Estève, and M. K. Oberthaler, Nonlinear atom interferometer surpasses classical precision limit, Nature (London) **464**, 1165 (2010).

[39] B. Lücke, M. Scherer, J. Kruse, L. Pezzè, F. Deuretzbacher, P. Hyllus, O. Topic, J. Peise, W. Ertmer, J. Arlt, L. Santos, A. Smerzi and C. Klempt, Twin matter waves for interferometry beyond the classical limit, Science **334**, 773 (2011).

[40] O. Hosten, N. J. Engelsen, R. Krishnakumar, and M. A. Kasevich, Measurement noise 100 times lower than the quantum-projection limit using entangled atoms, Nature (London) **529**, 505 (2016).

[41] I. Kruse, K. Lange, J. Peise, B. Lücke, L. Pezzè, J. Arlt, W. Ertmer, C. Lisdat, L. Santos, A. Smerzi, and C. Klempt, Improvement of an Atomic Clock Using Squeezed Vacuum, Phys. Rev. Lett. **117**, 143004 (2016).

[42] R. J. Sewell, M. Koschorreck, M. Napolitano, B. Dubost, N. Behbood, and M. W. Mitchell, Magnetic Sensitivity Beyond the Projection Noise Limit by Spin Squeezing, Phys. Rev. Lett. **109**, 253605 (2012).

[43] B. Braverman, A. Kawasaki, E. Pedrozo-Peñafiel, S. Colombo, C. Shu, Z. Li, E. Mendez, M. Yamoah, L. Salvi, D. Akamatsu, Y. Xiao, and V. Vuletić, Near-Unitary Spin Squeezing in ^{171}Yb, Phys. Rev. Lett. **122**, 223203 (2019).

[44] B. K. Malia, J. Martínez-Rincón, Y. Wu, O. Hosten, and M. A. Kasevich, Free Space Ramsey Spectroscopy in Rubidium with Noise Below the Quantum Projection Limit, Phys. Rev. Lett. **125**, 043202 (2020).

[45] S. S. Szigeti, O. Hosten, and S. A. Haine, Improving cold-atom sensors with quantum entanglement: Prospects and challenges, Appl. Phys. Lett. **118**, 140501 (2021).

[46] F. Anders, A. Idel, P. Feldmann, D. Bondarenko, S. Loriani, K. Lange, J. Peise, M. Gersemann, B. Meyer, S. Abend, N. Gaaloul, C. Schubert, D. Schlippert, L. Santos, E. Rasel, and C. Klempt, Momentum entanglement for atom interferometry, arXiv:2010.15796.

[47] L. Salvi, N. Poli, V. Vuletić, and G. M. Tino, Squeezing on Momentum States for Atom Interferometry, Phys. Rev. Lett. **120**, 033601 (2018).

[48] R. Geiger and M. Trupke, Proposal for a Quantum Test of the Weak Equivalence Principle with Entangled Atomic Species, Phys. Rev. Lett. **120**, 043602 (2018).

[49] A. Shankar, L. Salvi, M. L. Chiofalo, N. Poli, and M. J. Holland, Squeezed state metrology with Bragg interferome-

ters operating in a cavity, Quantum Sci. Technol. **4**, 045010 (2019).

[50] S. S. Szigeti, S. P. Nolan, J. D. Close, and S. A. Haine, High-Precision Quantum-Enhanced Gravimetry with a Bose-Einstein Condensate, Phys. Rev. Lett. **125**, 100402 (2020).

[51] H. Müller, S. W. Chiow, Q. Long, S. Herrmann, and S. Chu, Atom Interferometry with up to 24-Photon-Momentum-Transfer Beam Splitters, Phys. Rev. Lett. **100**, 180405 (2008).

[52] H. Ahlers, H. Müntinga, A. Wenzlawski, M. Krutzik, G. Tackmann, S. Abend, N. Gaaloul, E. Giese, A. Roura, R. Kuhl, C. Lämmerzahl, A. Peters, P. Windpassinger, K. Sengstock, W. P. Schleich, W. Ertmer, and E. M. Rase, Double Bragg Interferometry, Phys. Rev. Lett. **116**, 173601 (2016).

[53] J.-N. Siemß, F. Fitzek, S. Abend, E. M. Rasel, N. Gaaloul, and K. Hammerer, Analytic theory for Bragg atom interferometry based on the adiabatic theorem, Phys. Rev. A **102**, 033709 (2020).

[54] D. N. Aguilera, H. Ahlers, B. Battelier, A. Bawamia, A. Bertoldi, R. Bondarescu, K. Bongs, P. Bouyer, C. Braxmaier, L. Cacciapuoti, C. Chaloner *et al.*, STE-QUEST—test of the universality of free fall using cold atom interferometry, Classical Quantum Grav. **31**, 115010 (2014).

[55] J. M. Hogan, D. M. S. Johnson, and M. A. Kasevich, in *Atom Optics and Space Physics*, Proceedings of the International School of Physics "Enrico Fermi," Course CLXVIII, edited by E. Arimondo, W. Ertmer, and W. P. Schleich (IOS, Amsterdam, 2009), pp. 411-447.

[56] S. Hartmann, J. Jenewein, E. Giese, S. Abend, A. Roura, E. M. Rasel, and W. P. Schleich, Regimes of atomic diffraction: Raman versus Bragg diffraction in retroreflective geometries, Phys. Rev. A **101**, 053610 (2020).

[57] S. S. Szigeti, J. E. Debs, J. J. Hope, N. P. Robins, and J. D. Close, Why momentum width matters for atom interferometry with Bragg pulses, New J. Phys. **14**, 023009 (2012).

[58] E. B. Lee and L. Markus, *Foundations of Optimal Control Theory* (Wiley, New York, 1967).

[59] M. Kitagawa and M. Ueda, Squeezed spin states, Phys. Rev. A **47**, 5138 (1993).

[60] In our simulations, we specialize to the case of a BEC of rubidium-87 with $N = 10^3$ atoms. The s-wave scattering length is set equal to $a = 99.6a_0$, with a_0 the Bohr radius, and we define the wave vector $k_L = 2\pi/\lambda_L$ of the laser with $\lambda_L = 852$ nm. For the parameters of the rubidium atoms see http://steck.us/alkalidata.

[61] B. Yurke, S. L. McCall, and J. R. Klauder, SU(2) and SU(1, 1) interferometers, Phys. Rev. A **33**, 4033 (1986).

[62] D. J. Wineland, J. J. Bollinger, W. M. Itano, and D. J. Heinzen, Squeezed atomic states and projection noise in spectroscopy, Phys. Rev. A **50**, 67 (1994).

[63] P. Storey and C. Cohen-Tannoudji, The Feynman path integral approach to atomic interferometry. A tutorial, J. Phys. (France) II **4**, 1999 (1994).

[64] W. Li, T. He, and A. Smerzi, Multimode Kapitza-Dirac Interferometry with Trapped Cold Atoms, Phys. Rev. Lett. **113**, 023003 (2014).

[65] S. A. Haine, Quantum noise in bright soliton matterwave interferometry, New J. Phys. **20**, 033009 (2018).

[66] See Supplemental Material at http://link.aps.org/supplemental/10.1103/PhysRevA.103.L061301 for details.

[67] U. V. Poulsen and K. Mølmer, Quantum beam splitter for atoms, Phys. Rev. A **65**, 033613 (2002).

[68] K. Henderson, C. Ryu, C. MacCormick, and M. G. Boshier, Experimental demonstration of painting arbitrary and dynamic potentials for Bose-Einstein condensates, New J. Phys. **11**, 043030 (2009).

[69] R. Roy, A. Green, R. Bowler, and S. Gupta, Rapid cooling to quantum degeneracy in dynamically shaped atom traps, Phys. Rev. A **93**, 043403 (2016).

[70] L. Pezzè, A. Smerzi, G. P. Berman, A. R. Bishop, and L. A. Collins, Nonlinear beam splitter in Bose-Einstein-condensate interferometers, Phys. Rev. A **74**, 033610 (2006).

[71] U. V. Poulsen and K. Mølmer, Positive-P simulations of spin squeezing in a two-component Bose condensate, Phys. Rev. A **64**, 013616 (2001).

[72] A. Burchianti, C. D'Errico, L. Marconi, F. Minardi, C. Fort, and M. Modugno, Effect of interactions in the interference pattern of Bose-Einstein condensates, Phys. Rev. A **102**, 043314 (2020).

[73] D. Becker, M. D. Lachmann, S. T. Seidel, H. Ahlers, A. N. Dinkelaker, J. Grosse, O. Hellmig, H. Müntinga, V. Schkolnik, T. Wendrich, A. Wenzlawski *et al.*, Space-borne Bose-Einstein condensation for precision interferometry, Nature (London) **562**, 391 (2018).

[74] D. C. Aveline, J. R. Williams, E. R. Elliott, C. Dutenhoffer, J. R. Kellogg, J. M. Kohel, N. E. Lay, K. Oudrhiri, R. F. Shotwell, N. Yu and R. J. Thompson, Observation of Bose-Einstein condensates in an earth-orbiting research laboratory, Nature (London) **582**, 193 (2020).